

# Using the Discrete Dipole Approximation and Holographic Microscopy to Measure Rotational Dynamics of Non-spherical Colloidal Particles

Anna Wang<sup>a,1</sup>, Thomas G. Dimiduk<sup>b,1</sup>, Jerome Fung<sup>b</sup>, Sepideh Razavi<sup>c</sup>, Ilona Kretzschmar<sup>c</sup>, Kundan Chaudhary<sup>a</sup>, Vinodhan N. Manoharan<sup>a,b,\*</sup>

<sup>a</sup>*School of Engineering & Applied Sciences, Harvard University, 29 Oxford Street, Cambridge, MA 02138, USA*

<sup>b</sup>*Department of Physics, Harvard University, 17 Oxford Street, Cambridge, MA 02138, USA*

<sup>c</sup>*Department of Chemical Engineering, City College of City University of New York, NY 10031, USA*

## Abstract

We present a new, high-speed technique to track the three-dimensional translation and rotation of non-spherical colloidal particles. We capture digital holograms of micrometer-scale silica rods and sub-micrometer-scale Janus particles freely diffusing in water, and then fit numerical scattering models based on the discrete dipole approximation to the measured holograms. This inverse-scattering approach allows us to extract the position and orientation of the particles as a function of time, along with static parameters including the size, shape, and refractive index. The best-fit sizes and refractive indices of both particles agree well with expected values. The technique is able to track the center of mass of the rod to a precision of 35 nm and its orientation to a precision of 1.5°, comparable to or better than the precision of other 3D diffusion measurements on non-spherical particles. Furthermore, the measured translational and rotational diffusion coefficients for the silica rods agree with hydrodynamic predictions for a spherocylinder to within 0.3%. We also show that although the Janus particles have only weak optical asymmetry, the technique can track their 2D translation and azimuthal rotation over a depth of field of several micrometers, yielding independent measurements of the effective hydrodynamic radius that agree to within 0.2%. The internal and external consistency of these measurements validate the technique. Because the discrete dipole approximation can model scattering from arbitrarily shaped particles, our technique could be used in a range of applications, including particle tracking, microrheology, and fundamental studies of colloidal self-assembly or microbial motion.

**Keywords:** light scattering, digital holography, colloids, discrete dipole approximation, non-spherical, diffusion

## 1. Introduction

Measurements of the dynamics of colloidal particles are key to understanding the mechanisms of colloidal aggregation [1] and self-assembly [2]. Microscopic measurements of the diffusion of individual particles can furthermore be used to infer interactions between particles [3] as well as the local rheological properties of the medium in which the particles are suspended [4]. Most microscopic measurements are constrained to two dimensions because of the limited depth of field of wide-field microscopy [5]. Confocal microscopy can be used to capture three-dimensional (3D) dynamics of spherical and non-spherical particles [6, 7], but the time required to scan the beam through a 3D sample limits these measurements to large particles or particles in a viscous fluid.

Holographic microscopy is an alternative technique that can in principle capture 3D colloidal dynamics with acquisition times orders of magnitude smaller than those of confocal microscopy. In a holographic microscope, light from a coherent source scatters from the sample and interferes with a reference wave—which can simply be the transmitted, undiffracted beam.

The interference pattern, or hologram, contains phase information about the scattered wave and can be used to determine the 3D position of the particle. Because holograms can be captured as fast as a camera allows and then processed offline, the technique can be used to probe millisecond or even microsecond dynamics. The 3D information is typically recovered through optical or numerical reconstruction [8]. Cheong and co-workers [9] used this method to track the 3D translation and rotation of a high-aspect-ratio (1:25) copper oxide nanoparticle through numerical reconstruction and a skeletonization procedure. However, for wavelength-scale particles the precision of reconstructions is limited owing to distortions in the reconstructed volume [10, 11].

We demonstrate a precise way to measure the dynamics of wavelength-scale, non-spherical colloidal particles from holographic measurements. Our approach, which uses an inverse-scattering analysis rather than reconstruction, follows the work of Lee and coworkers [12], who showed that fitting a Lorenz-Mie scattering solution to a measured hologram yields nanometer-scale-precision measurements of the positions of spherical particles. Researchers from our group, including Fung and coworkers [13, 14] and Perry and coworkers [15] later showed that the translational, rotational, vibrational, and nonequilibrium dynamics of several interacting wavelength-scale spheres could be measured with high precision by fitting

\*Corresponding author

Email address: vnm@seas.harvard.edu (Vinodhan N. Manoharan)

<sup>1</sup>A. Wang and T.G. Dimiduk contributed equally to this work.

Mackowski and Mishchenko's T-matrix solution [16] to holograms of multiple colloidal particles. All of these measurements were limited to spheres, or collections of spheres, because the fitting technique requires a solution for the scattered field, and exact solutions are known for very few particle morphologies.

One can, however, perform approximate numerical scattering calculations for a wide variety of particles using the Discrete Dipole Approximation (DDA) of Purcell and Pennypacker [17]. We show that numerical scattering calculations using the DDA can be fit to holograms of non-spherical particles, allowing us to track 3D translational and rotational dynamics at high precision, even for particles with subtle asymmetries. We use these measurements to determine translational and rotational diffusion coefficients and show that the measured values agree well with theoretical calculations, validating the technique. Although DDA calculations are orders of magnitude slower than calculations of exact scattering solutions, parallelization of the scattering calculations and the fitting algorithm can significantly reduce the analysis time.

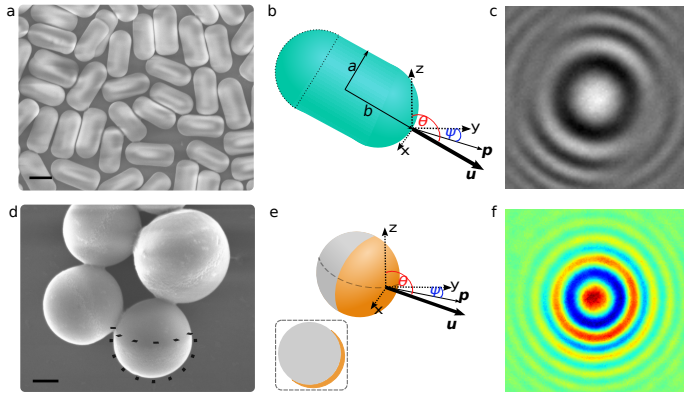


Figure 1: The non-spherical particles used in our experiments. Top row, silica rods; bottom row, Janus particles consisting of a polystyrene sphere coated with a 50-nm-thick layer of  $\text{TiO}_2$ . The orientation of both types of particles is defined by the orientational unit vector  $\mathbf{u}$  and its projection onto the  $x-y$  plane,  $\mathbf{p}$ . The  $z$ -axis coincides with the direction of the incident plane wave illumination. (a) Scanning electron micrograph of the rods. Scale bar is  $1\ \mu\text{m}$ . (b) The rod is modeled as a spherocylinder with semi-minor-axis length  $a$  and semi-major-axis length  $b$ . (c) Measured hologram of a single rod. (d) Scanning electron micrograph of the Janus particles. The dotted line outlines the  $\text{TiO}_2$  cap. Scale bar is  $300\ \text{nm}$ . (e) The Janus particle is modeled as a plain polystyrene sphere with a hemispherical cap of  $\text{TiO}_2$  (orange). A cross section perpendicular to the equator is also shown. (f) Measured hologram of a Janus particle, shown in false color to highlight asymmetry.

## 2. Experimental Methods

We use two types of anisotropic particles in this study: silica rods and polystyrene/ $\text{TiO}_2$  Janus particles suspended in water (Figure 1). The silica rods are synthesized using a modified one-pot method recently reported by Kuijk and coworkers [18, 19]. In the initial growth step, we make silica rods with a length ( $L$ ) of  $1.45 \pm 0.06\ \mu\text{m}$  and diameter ( $D$ ) of  $0.29 \pm 0.02\ \mu\text{m}$ , which are then used as seeds in subsequent growth steps [20] to produce the final silica rods. The size of the

rods, as determined by scanning electron microscopy (SEM), is  $1.0 \pm 0.2\ \mu\text{m}$  (minor axis) by  $2.0 \pm 0.2\ \mu\text{m}$  (major axis) (Figure 1a). We fabricate the Janus particles by depositing  $50\ \text{nm}$  of  $\text{TiO}_2$  onto sulfate-terminated polystyrene (PS) particles (Invitrogen), as described in reference [21]. The polystyrene particle diameter, as determined by SEM, is  $900 \pm 100\ \text{nm}$  (neglecting anomalously large particles). The  $\text{TiO}_2$  cap covers approximately one hemisphere of the particle, as shown in Figure 1d.

For holographic imaging, we suspend the particles in deionized water at approximately  $10^{-5}$  volume fraction and place them in sample cells consisting of two No. 1 glass coverslips (VWR) separated and sealed by vacuum grease (Dow Corning). To validate the DDA method, we also image a  $0.95\text{-}\mu\text{m}$ -radius polystyrene sphere (Invitrogen) diffusing in a 54% v/v glycerol solution.

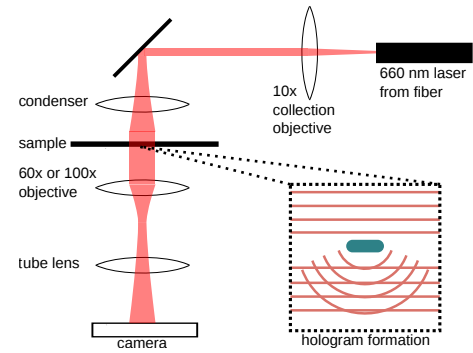


Figure 2: Schematic of our digital in-line holographic microscope. A series of lenses, including the condenser, shapes light from a 660 nm laser diode (Opnext HL6545MG) into a plane wave to illuminate the sample. An objective collects the transmitted light and light scattered from the sample, and a high-speed camera (Photon Focus) captures the hologram formed by the interference between scattered and transmitted waves.

We capture holograms with a digital holographic microscope built on a Nikon (TE2000-E) inverted microscope, as shown in Figure 2 and described in detail in [13, 22]. When imaging the Janus particles we use a  $100\times$  oil-immersion objective (Nikon) with a high numerical aperture (1.40) that allows us to maximize detail in the holograms. When imaging the silica rods, which sediment rapidly owing to their density, we use a  $60\times$  water-immersion objective (Nikon), which has a lower numerical aperture (1.20) but a larger working distance that allows us to capture longer trajectories. To obtain true bulk-diffusion measurements, we retain data only from particles that remain at least  $20\ \mu\text{m}$  away from the sample cell boundaries throughout the trajectory.

In a typical experiment we use  $50\ \text{mW}$  of laser power and a  $0.015\ \text{ms}$  exposure time per camera frame for the  $60\times$  lens or  $0.05\ \text{ms}$  for the  $100\times$  lens. These exposure times are short enough to minimize blurring due to Brownian motion. We capture holograms with a Photon Focus MVD-1024E-160 camera at 100 frames per second, store them in RAM using a frame grabber (EPIX PIXCI E4), and then save to disk for further processing. For each trajectory we also record a background image from the same region of the sample cell before or after the particle is present to account for scattering and illumination defects in the optical train.

### 3. Fitting holograms using the DDA

In contrast to holograms of spheres, holograms of non-spherical particles do not have azimuthal symmetry about the central maximum (see Figure 1c, f). The azimuthal asymmetry encodes information about the particle shape and orientation, while the radial spacing of the interference fringes encodes the particle position. To quantitatively extract this information, we fit a scattering model to the holograms.

In our fitting procedure, we compute holograms from a model, compare the computed holograms to experimentally recorded ones, and iterate until the model matches the data. To compute the hologram, we model the physical process of hologram formation: the interference of scattered and reference fields. In an inline hologram, the reference field is approximately equal to the incident field  $\mathbf{E}_i$ , as long as the density of scatterers is low. In our experiments, we work at low concentrations of particles, so that we can assume  $\mathbf{E}_i$  is a constant plane wave. The observed intensity is therefore

$$I_{\text{holo}} = |\mathbf{E}_i + \mathbf{E}_s|^2, \quad (1)$$

where  $\mathbf{E}_s$  is the scattered field, which we must compute to simulate the hologram. Previous work [12, 13, 15, 22] used numerical implementations of the Lorenz-Mie solution or a multi-sphere superposition solution [16] to compute  $\mathbf{E}_s$ . However, these exact solutions are limited to spheres or collections of spheres. For the non-spherical particles used here, we must compute  $\mathbf{E}_s$  approximately. We do this using the discrete dipole approximation, as implemented by the open-source scattering code ADDA [23].

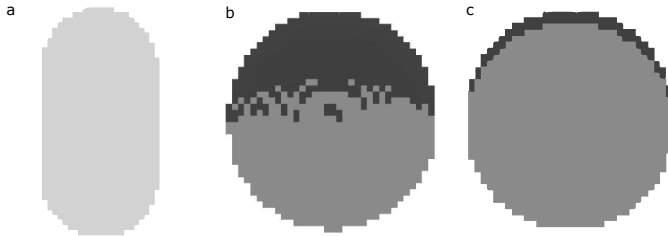


Figure 3: Voxelations of the particles. White represents vacuum, light gray is silica, medium gray is polystyrene and dark gray is  $\text{TiO}_2$ . Each dipole is represented by a square. (a) Side view of a rod with a dipole size of 44 nm, a semi-minor-axis length of 500 nm and a semi-major-axis length of 1  $\mu\text{m}$ . (b) Side view of a Janus particle with a dipole size of 24 nm, inner particle radius of 439 nm and a maximum cap thickness of 50 nm. (c) Cross section of the same Janus particle.

In the DDA, a scatterer is represented as an array of point dipoles. Therefore the first step of our data analysis is to discretize the particle, dividing it into an array of voxels (volumetric pixels). To ensure validity of the DDA, we discretize the scatterer using at least 10 dipoles per wavelength in the scattering medium, as recommended by the ADDA documentation [23]. The voxelations of both particles are shown in Figure 3. For the Janus particle, the dipole size is comparable to the thickness of the  $\text{TiO}_2$  layer; but because the shape and size of the cap varies from particle to particle, a smaller dipole size would not necessarily increase accuracy.

To compute a hologram, we calculate the scattering angles for each pixel in the detector, then invoke ADDA to compute the scattering matrix of the voxelated particle at each scattering angle. We obtain the electric field  $\mathbf{E}_s(i, j)$  at each pixel  $(i, j)$  on the detector from the scattering matrices, angles, and distances. Finally, we numerically interfere the computed  $\mathbf{E}_s(i, j)$  with  $\mathbf{E}_i(i, j)$ , a plane wave, to obtain the hologram. All of these steps are implemented in our open-source hologram processing code, HoloPy (<http://manoharan.seas.harvard.edu/holopy/>).

Once we have created a DDA scattering model for a particle, we use nonlinear minimization to fit the model to measured, background-divided, normalized holograms, thereby obtaining measurements of the positions, refractive index, and geometrical parameters of individual particles. Formally, we use the Levenberg-Marquardt algorithm to minimize the objective function

$$f(\{p\}) = \sum_{i,j} |I_{\text{measured}}(i, j) - I_{\text{computed}}(i, j; \{p\})|^2 = \chi^2 \quad (2)$$

where

$$I_{\text{measured}} = \frac{I_{\text{data}}}{I_{\text{background}}} \frac{\bar{I}_{\text{background}}}{\bar{I}_{\text{data}}},$$

and  $\{p\}$  is the set or a subset of the parameters used by the DDA model to calculate the scattering from the particle. The minimization typically requires several iterations to converge. We then use the fitted position and orientations obtained from a time-series of holograms to compute the diffusion coefficients.

Because the two types of particles have different geometries, we must use different sets of parameters to model them. We model the rod, which has rounded ends as shown in Figure 1a, as a dielectric spherocylinder with refractive index  $n$ , hemisphere radius  $a$  (equal to the length of the semi-minor-axis), and semi-major-axis length  $b$ . The full set of parameters is

$$\{p_{\text{rod}}\} = \{\mathbf{r}, n, a, b, \theta, \psi, \alpha\}, \quad (3)$$

where  $\mathbf{r}$  is the center of mass position,  $\theta$  and  $\psi$  are Euler angles describing particle orientation (see Figure 1b), and  $\alpha$  is a normalization constant [12]. We model the Janus particle (Figure 1d) as a dielectric sphere with refractive index  $n_{\text{PS}}$  and radius  $a_{\text{Janus}}$  capped by a hemispherical dielectric shell with index  $n_{\text{TiO}_2}$  and thickness  $t$ . Here the set of parameters is

$$\{p_{\text{Janus}}\} = \{\mathbf{r}, n_{\text{PS}}, n_{\text{TiO}_2}, a_{\text{Janus}}, t, \theta, \psi, \alpha\}, \quad (4)$$

where  $\mathbf{r}$  is the center of the sphere,  $\theta$  and  $\psi$  are the Euler angles shown in Figure 1e, and  $\alpha$  is again a normalization constant.

To assess the validity of the fits, we examine the coefficient of determination,  $R^2$ , which measures how much of the variation from the mean value of one hologram is captured in another:

$$R^2 = 1 - \frac{\sum_{i,j} |I_1(i, j) - I_2(i, j)|^2}{\sum_{i,j} |I_1(i, j) - \bar{I}_1|^2}, \quad (5)$$

where  $\bar{I}_1 = 1$  is the mean value of the normalized hologram.  $R^2$  is a useful quantity because unlike  $\chi^2$ , which is sensitive to the amplitude of the hologram fringes, the  $R^2$  values for good fits do

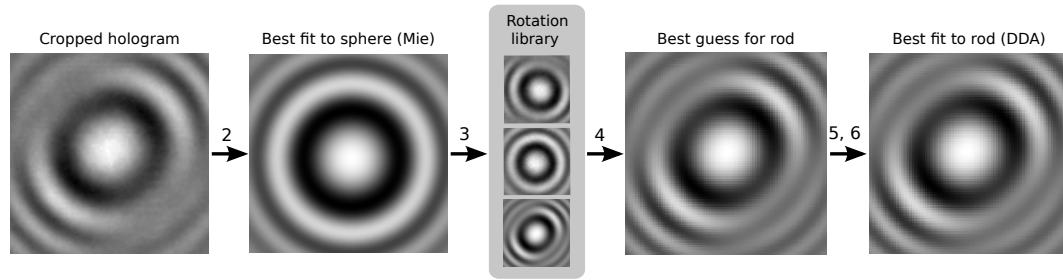


Figure 4: Procedure for fitting DDA models to experimental holograms of non-spherical particles to extract position and orientation. The numbers refer to the steps in the text.

not vary markedly across experimental systems with different scattering cross sections [24]. We use  $R^2$  to assess how well DDA reproduces the results of exact Lorenz-Mie calculations for holograms of spheres and to assess how well the holograms from our model match data from experiments.

Because DDA calculations take at least an order of magnitude longer than Lorenz-Mie calculations for scatterers of the same size, we aim to fit all the frames in parallel. This goal is complicated by convergence requirements. In practice, we have found that the minimization does not converge unless the initial guess for  $\{p\}$  is close to the global minimum of the objective function. Therefore our usual procedure [13, 14] is to fit the frames sequentially: we use reconstruction to manually obtain an initial guess for the first frame of the trajectory and then use the best-fit result for each frame as the initial guess for the next. Here such a process would take too long. A DDA calculation takes on the order of 30 seconds on a single CPU; since about 200 such calculations are required for each minimization to converge, it would take 20 weeks to sequentially fit a 2000-frame trajectory. We therefore use the procedure described below and illustrated in Figure 4 to obtain the initial guesses for each frame and fit the frames in parallel:

1. *Select the most asymmetric region:* The particle orientation is primarily encoded in the rotational asymmetry of a hologram. We maximize sensitivity to the particle orientation by cropping the hologram to leave only the most asymmetric region, the first fringe or two around the central maximum. We use a Hough transform-based algorithm [25] to locate the center of the hologram. For our experiments the first fringe is located within a  $140 \times 140$  pixel area.
2. *Find approximate position with a Lorenz-Mie fit:* We obtain an estimate of the particle's position by approximating it as a sphere with parameters  $\{p\} = \{\mathbf{r}_{\text{Mie}}, n, a_{\text{Mie}}, \alpha\}$  and fitting the Lorenz-Mie solution to the hologram. This fit is very fast (order of 10 seconds per frame) and although  $\chi^2$  is large,  $\mathbf{r}_{\text{Mie}}$  provides a good initial guess for the position of the particle's center.
3. *Make rotation library:* We use the DDA to calculate holograms of the non-spherical particle over a range of Euler angles  $\theta, \psi$ , assuming a center position  $\mathbf{r}_{\text{Mie}}$ .
4. *Use library to guess angles:* We compare this library to the experimental hologram and determine the Euler angles  $\theta, \psi$  that yield the highest  $R^2$  value.

5. *Initial DDA fit:* We fit the DDA model to the measured hologram using the guess for  $\mathbf{r}_{\text{Mie}}$  from step 2,  $\theta, \psi$  from step 4, bulk values for the index or indices, and an estimate of the geometrical parameters  $a$  and  $b$  or  $a_{\text{Janus}}$  and  $t$  from SEM images. We allow all parameters to vary during the fit. In this step, we fit the first 500 frames of a trajectory, discard the fits that fail to converge, then calculate the average best-fit refractive indices and radii.
6. *Final DDA fit:* Because the particle's physical properties should not change across a trajectory, we fix the refractive indices and radii to the average values from step 5 and fit the cropped holograms for an entire trajectory to obtain the position and orientation as a function of time.

This procedure removes the serial dependency between the frames in a time series, allowing us to send each frame in the initial (step 5) and final (step 6) DDA fits to an individual CPU on a computing cluster. However, removing the serial dependency potentially introduces artifacts in the trajectories of the particles, since the results from each frame are not used to constrain the results of the next. We must therefore detect and correct spurious fit results.

There are two kinds of errors. The first arises because the rod particles are symmetric, having two degenerate orientational unit vectors pointing in opposite directions. In a trajectory constructed from a series of parallel fits, the fitted orientational unit vector may therefore flip almost  $180^\circ$  between frames. Using the probability density function for rotational displacements described in reference [14] and an estimated rotational diffusion coefficient  $D_{\text{est}} = 0.3 \text{ s}^{-1}$ , we estimate that the probability of a  $90^\circ$  or greater change in angle between frames is zero, to within machine precision. Therefore we can correct artificial flips by examining pairs of frames in the trajectory and flipping the vector in the second frame by  $180^\circ$  if the angle changes by more than  $90^\circ$  between frames.

The second type of spurious fit result arises because the Levenberg-Marquardt algorithm is sensitive to noise. Depending on the initial guess, a fit can converge to a secondary minimum in which the orientational unit vector  $\mathbf{u}$  points in a direction mirrored about the x-y plane from that of the previous frame. A small number of these bad fits systematically increases the apparent diffusion coefficient.

We therefore reject contributions to the mean-square displacement where the probability of the measured angular dis-



placement is less than 0.0001. Again, we calculate the probability of observing a given displacement using the probability density function for rotational displacements described in reference [14] and an estimated rotational diffusion coefficient  $D_{\text{est}} = 0.3 \text{ s}^{-1}$ . Using  $D_{\text{est}} = 0.2 \text{ s}^{-1}$  or  $D_{\text{est}} = 0.4 \text{ s}^{-1}$  changes the coefficients extracted from the data by less than 7%, an effect which we include in the error on the measured diffusion coefficients. This procedure eliminates poor fit results while minimizing the bias of results toward our estimated diffusion coefficient.

## 4. Results and Discussion

We demonstrate the validity and usefulness of the DDA as a tool for holography and particle tracking through a series of experimental and computational tests. First we compare the results of DDA and Lorenz-Mie calculations for scattering from spherical particles, which the Lorenz-Mie solution models exactly. Next we fit the DDA model to holograms of a rod and a Janus particle, and we obtain translational and rotational diffusion coefficients from the mean-square displacements measured across time-series of holograms. We compare the measured diffusion coefficients to predicted values to demonstrate that we accurately and precisely capture the particle motion.

### 4.1. Validation of DDA calculations and fits

We first examine how the approximations involved in our DDA implementation affect the quality of the fits and calculated holograms. To do this, we compare holograms of spheres calculated with our DDA model to those calculated from the Lorenz-Mie solution. We are interested in two effects: first, how aliasing introduced by the voxelation affects the precision of fitting holograms and, second, how the absence of a near-field calculation in ADDA affects the accuracy of the holograms. By “near field” we mean the part of the scattered field that does not follow an asymptotic  $1/r$  decay. ADDA calculates only the asymptotic portion of the scattered field. In previous work [13, 24] we found that it was necessary to include the full radial dependence of  $\mathbf{E}_s$  to accurately fit holograms of particles close to the focal plane.

We test the validity of the scattering model, including our voxelation scheme, by fitting the DDA model and the Lorenz-Mie solution to 893 measured holograms of a 0.95- $\mu\text{m}$ -radius polystyrene sphere (Invitrogen) freely diffusing in a 54% v/v glycerol solution. We fix both the refractive index and radius of the particle and allow only the center position of the sphere to vary. Throughout the trajectory, the particle remains 15  $\mu\text{m}$  to 18  $\mu\text{m}$  from the focal plane.

We find that the best-fit  $x$ - and  $y$ -coordinates obtained by fitting the DDA model differ negligibly ( $0.3 \pm 0.1 \text{ nm}$ ) from those obtained from Lorenz-Mie, while the best-fit  $z$ -coordinates differ by  $194 \pm 1 \text{ nm}$ , a significant offset. This difference in apparent axial position might arise from voxelation errors or the asymptotic approximation for the radial dependence of the scattered field. The Lorenz-Mie model includes non-asymptotic corrections for the scattered field, while the DDA model does not.

The offset in the  $z$ -coordinate does not affect our dynamical measurements, which depend only on the displacement of the particle, not its absolute position. We find that the total displacements  $\|\mathbf{r}(t) - \mathbf{r}(0)\|$  for the DDA and Lorenz-Mie models, as calculated from the best-fit coordinates for the entire trajectory, agree to within 0.5 nm (Figure 5a) for most of the frames analyzed. The maximum deviation in displacement is 2 nm, which is within the reported accuracy of holographic measurements based on inverse-scattering analysis [12]. Thus the systematic error in the absolute particle position appears to cancel when calculating the displacement, and the resulting displacement measurements are nearly as precise as those obtained by fitting the data to the exact Lorenz-Mie solution.

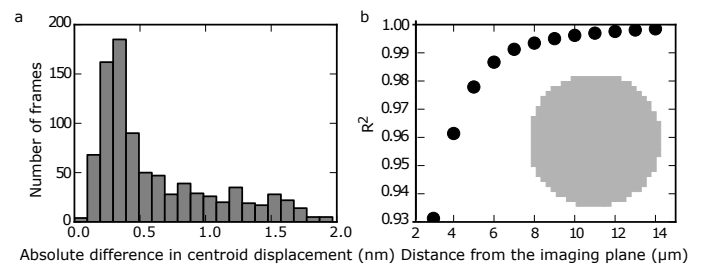


Figure 5: Comparison of the DDA model and Lorenz-Mie solution for fitting holograms of a single sphere. (a) Histogram of differences between displacements of a 950-nm-radius diffusing sphere measured by fitting the DDA and Lorenz-Mie models to measured holograms. (b)  $R^2$  for pairs of holograms calculated from the exact Lorenz-Mie solution and the DDA model of a 450-nm-radius sphere at various distances from the imaging plane. Inset: voxelation of the 450-nm-radius sphere used in the DDA model. The voxel size is 34 nm. The particle refractive index is 1.585.

To further examine the impact of the asymptotic approximation for the scattered field, we compare holograms computed from the DDA model and Lorenz-Mie solutions for a 450-nm-radius sphere as a function of distance from the focal plane. The agreement between the two models, as measured by the  $R^2$  value, increases with distance from the imaging plane, as shown in Figure 5b. These data suggest that near-field effects start to vary significantly with distance when the particle is 5  $\mu\text{m}$  or less from the focal plane. To ensure the validity of our DDA fits, we take all measurements with the particle at least 5  $\mu\text{m}$  from the imaging plane.

As another check on the validity of the technique, we examine the average of fitted values for the optical properties and sizes of our non-spherical particles. We find  $n = 1.495 \pm 0.012$  for the rod,  $n_{\text{PS}} = 1.581 \pm 0.046$  for the polystyrene particle and  $n_{\text{TiO}_2} = 2.74 \pm 0.23$  for the shell of the Janus particle, all of which are close to bulk values for the materials. The best-fit dimensions of the rod are  $2a = 1.002 \pm 0.037 \mu\text{m}$  and  $2b = 2.158 \pm 0.143 \mu\text{m}$ , in agreement with the measurements from SEM. The fitted dimensions of a Janus particle are  $a_{\text{Janus}} = 443 \pm 20 \text{ nm}$ , in excellent agreement with the SEM images, and  $t = 47 \pm 8 \text{ nm}$ , in good agreement with the expected value based on the  $\text{TiO}_2$  deposition process.

Qualitatively, the trajectories of the particles we obtain by fitting the DDA model to time-series of holograms are consistent with stochastic Brownian motion (Figure 6). Furthermore, the

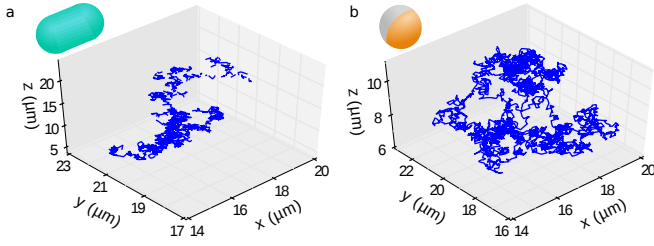


Figure 6: Trajectories of particles as determined from DDA fits. (a) Rod trajectory captured at 100 frames per second for 20 seconds. (b) Janus particle trajectory captured at 100 frames per second for 30 seconds.

rod appears to sediment at  $0.9 \mu\text{m/s}$  whereas the Janus particle diffuses about a steady height. This behavior agrees qualitatively with our expectations for the two systems: the rod should sediment more rapidly because the density difference between the rod and solvent is about three times larger than that of the Janus particle, and the rod has about three times the volume of the Janus particle.

Finally, to quantitatively investigate the validity of the DDA fits, we determine the rotational and translational diffusion coefficients from the data and compare them to theoretically predicted values, as described in the following sections.

#### 4.2. Rods

When viewed in the laboratory frame, the motion of a rod is complicated because the viscous drag along any laboratory axis depends on the orientation of the particle. But in the frame of the particle, translational diffusion can be broken down into two components, one parallel to the long axis of the particle ( $\parallel$ ) and the other along either of the two principal axes perpendicular to the long axis ( $\perp$ ). Due to the optical symmetry of the particle, we cannot observe rotations about the major axis. We can therefore measure only one rotational diffusion coefficient, corresponding to rotation about either of the two degenerate principal axes that are coincident with the minor axis.

To measure these diffusion coefficients, we use the best-fit positions obtained from the holograms to calculate the translational and angular mean-square displacements in the particle frame as a function of lag time. We average these displacements over time and calculate the uncertainties associated with these averages using a block decorrelation method [26]. Finally, we fit the mean-square displacements using the calculated uncertainties as weights. The uncertainties are represented as error bars in the figures. In the following sections we report the formulas used to calculate and fit the displacements, as well as our measured and predicted values for the diffusion coefficients.

##### 4.2.1. Theoretical predictions

For clarity, we denote all predicted values of diffusion coefficients with a prime symbol ( $'$ ). The diffusion coefficients of a spherocylinder can be expressed as power series in the aspect ratio  $\omega = b/a$ , as discussed in the appendix of reference [27],

which is adapted from references [28] and [29]:

$$D'_t \approx \frac{k_B T}{6\pi\eta b} (\ln \omega + 0.3863 + 0.6863/\omega - 0.0625/\omega^2 - 0.01042/\omega^3 - 0.000651/\omega^4 + 0.0005859/\omega^5) \quad (6)$$

where  $D_t = (2D_\perp + D_\parallel)/3$ . We compare our results to the predicted value for  $D_t$ , which is a linear combination of the measured diffusion coefficients. From the same reference, we obtain the rotational diffusion coefficient:

$$D'_r \approx \frac{3k_B T}{8\pi\eta b^3} \left( \ln \omega + 2 \ln 2 - \frac{11}{6} + \frac{\ln 2}{\ln(1+\omega)} \left[ \frac{1}{3} - 2 \ln 2 + \frac{11}{6} - |\mathbf{a}| \right] + \mathbf{a} \cdot \boldsymbol{\Omega} \right) \quad (7)$$

where

$$\mathbf{a} = [13.04468, -62.6084, 174.0921, -218.8365, 140.26992, -33.27076],$$

and

$$\boldsymbol{\Omega} = [\omega^{-1/4}, \omega^{-2/4}, \omega^{-3/4}, \omega^{-4/4}, \omega^{-5/4}, \omega^{-6/4}].$$

Because the rods are slightly asymmetric—flatter on one end of the rod than the other (see Figure 1a)—we also compare our results for the translational and rotational diffusion coefficients to theoretical predictions for a cylinder with flat ends [30]:

$$D'_\perp \approx \frac{k_B T}{8\pi\eta b} (\ln \omega + 0.839 + 0.185/\omega + 0.233/\omega^2) \quad (8)$$

$$D'_\parallel \approx \frac{k_B T}{4\pi\eta b} (\ln \omega - 0.207 + 0.980/\omega - 0.133/\omega^2) \quad (9)$$

$$D'_r \approx \frac{3k_B T}{8\pi\eta b^3} (\ln \omega - 0.662 + 0.917/\omega - 0.050/\omega^2). \quad (10)$$

We use the laboratory temperature and uncertainty,  $21 \pm 2^\circ\text{C}$ , the corresponding viscosity for water, and the dimensions of the particle from the hologram fits to calculate the predicted diffusion coefficients and their uncertainties. As the values of rod's fitted dimensions are not normally distributed, we do not include them when propagating the errors.

##### 4.2.2. Translational diffusion

To extract translational diffusion coefficients from the data, we first calculate the mean-square displacements parallel and perpendicular to the major axis. For short lag times  $\tau$  we calculate

$$\Delta r_\parallel^2(\tau) = \langle ((\mathbf{r}(t+\tau) - \mathbf{r}(t)) \cdot \mathbf{u}(t))^2 \rangle = 2D_\parallel\tau + 2\epsilon_\parallel^2 \quad (11)$$

$$\Delta r_\perp^2(\tau) = \langle |(\mathbf{r}(t+\tau) - \mathbf{r}(t)) \times \mathbf{u}(t)|^2 \rangle = 4D_\perp\tau + 4\epsilon_\perp^2 \quad (12)$$

where the angle brackets denote a time average over all contributing pairs from a single trajectory. We then determine the diffusion coefficients  $D_\parallel$  and  $D_\perp$  and measurement errors  $\epsilon_\parallel$  and  $\epsilon_\perp$  by fitting a linear model to the measured mean-square displacements.

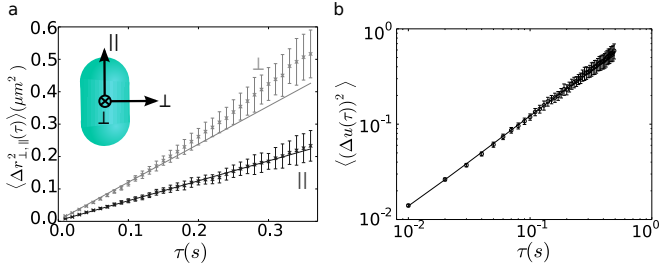


Figure 7: Measured mean-square displacements for the silica rods. (a) Mean-square displacements parallel and perpendicular to the major axis. The solid lines are fits to  $2D_{\parallel}\tau + 2\epsilon_{\parallel}^2$  and  $4D_{\perp}\tau + 4\epsilon_{\perp}^2$ . (b) Mean-square displacement of the orientational unit vector  $\mathbf{u}$ . The solid line is a fit to the function  $2 - 2\exp(-2D_r\tau) + 2\epsilon_r^2$ .

Our measured results agree with those predicted by the spherocylinder model. We obtain  $D_{\parallel} = 0.307 \pm 0.028 \mu\text{m}^2/\text{s}$ ,  $D_{\perp} = 0.293 \pm 0.025 \mu\text{m}^2/\text{s}$  and  $D_r = 0.298 \pm 0.026 \mu\text{m}^2/\text{s}$  (see Figure 7 and Table 1). These values are larger than the predictions for a cylinder with flat ends ( $D_{\parallel}' = 0.301 \pm 0.013 \mu\text{m}^2/\text{s}$  and  $D_{\perp}' = 0.265 \pm 0.012 \mu\text{m}^2/\text{s}$ ) but agree quantitatively with the spherocylinder model ( $D_{\parallel}' = 0.297 \pm 0.016 \mu\text{m}^2/\text{s}$ ), suggesting that the rods are better modeled as spherocylinders.

The fit, which is constrained by the small uncertainties at shorter lag times, falls outside the error range for the perpendicular direction at larger lag times (Figure 7). However, the fit for the parallel component is well within the error bars throughout the entire range of lag times. The apparent augmented motion in the perpendicular direction may be due to radiation pressure from the incident beam or coupling between sedimentation and diffusion [31].

The measured ratio  $D_{\parallel}/D_{\perp} = 1.05 \pm 0.04$  depends only on the aspect ratio of the particle. Our value is smaller than that predicted by the cylinder model ( $D_{\parallel}'/D_{\perp}' = 1.13$ ). The small discrepancy in the measured and predicted values of  $D_{\parallel}/D_{\perp}$  is not surprising, given how much the measured  $D_{\parallel}$  and  $D_{\perp}$  values differ individually from those predicted by the cylinder model. We are not able to calculate  $D_{\parallel}/D_{\perp}$  for the spherocylinder model because we do not have explicit expressions for the two individual components. In general, however, we expect  $D_{\parallel}/D_{\perp}$  to be of order unity for particles that have an aspect ratio of 1:2. Therefore our measured value is physically reasonable.

From the linear fit to the mean-square displacement, we find that the precision to which we track the rod's center of mass is 35 nm or better ( $\epsilon_{\parallel} = 28.3 \text{ nm}$  and  $\epsilon_{\perp} = 35.4 \text{ nm}$ ), which is around the same size as one voxel (approximately 35 nm). Though about an order of magnitude lower than the precision to which single spheres can be tracked, this precision compares favorably with that of tracking more complex scatterers, such as spheres in clusters [13, 15].

#### 4.2.3. Rotational diffusion

To determine the rotational diffusion coefficient, we first calculate the mean-square displacement of the orientational unit vector  $\mathbf{u}$ :

$$\Delta \mathbf{u}^2(\tau) = \langle (\mathbf{u}(t + \tau) - \mathbf{u}(t))^2 \rangle = 2(1 - e^{-2D_r\tau}) + 2\epsilon_r^2. \quad (13)$$

We then fit  $\Delta \mathbf{u}^2(\tau)$  to find the diffusion coefficient  $D_r$  and its angular uncertainty  $\epsilon_r$ .

We find  $D_r = 0.311 \pm 0.034 \text{ rad}^2/\text{s}$  (Figure 7), which is larger than that predicted by the cylinder model ( $D_r' = 0.205 \pm 0.008 \text{ rad}^2/\text{s}$ ) but in quantitative agreement with the spherocylinder model ( $D_r' = 0.311 \pm 0.017 \text{ rad}^2/\text{s}$ ). The error obtained from the fits is  $\epsilon_r = 0.0265 \text{ rad}$ , yielding an angular tracking precision of  $1.5^\circ$ . Like the translation results, these results suggest that the rods are modeled well, both hydrodynamically and optically, as spherocylinders. Furthermore the tracking precision is better than that reported for nanorods using reconstructions (approximately  $3^\circ$ ) and dimers using multisphere superposition solutions ( $3.4^\circ$ ) [9, 13].

#### 4.3. Janus particles

We find that it is more difficult to fit our scattering model to the Janus particle holograms, as they are only weakly asymmetric. In particular, we find that the best-fit polar angle  $\theta$  is often spurious. There are two local minima in the objective function, corresponding to two polar angles reflected about the x-y plane, and two different z-coordinates: if we calculate a hologram of a Janus particle with  $\theta = 0$  and  $z = 8.0 \mu\text{m}$ , and we fit to it using an initial guess of  $\theta \geq \pi/2$ , the fit converges to  $\theta = \pi$  and  $z = 7.811 \mu\text{m}$ . We find an  $R^2 = 0.9997$  and a per-pixel  $\chi^2$  of  $3.8 \times 10^{-6}$ , showing that the best-fit and original holograms are essentially identical. These calculations suggest that errors in the best-fit polar angle are correlated with those of the z-coordinate. Noise in the hologram could therefore cause the fitting algorithm to converge to either local minimum. Indeed, we estimate our noise floor for the 8-bit images to be at least an order of magnitude larger at  $(1/255)^2 = 1.5 \times 10^{-5}$  [14]. Increasing the asymmetry of the hologram, for example by increasing the aspect ratio or using a metal-coated Janus particle as in reference [5], should eliminate this problem. But for the results shown below, we determine dynamical data only from the best-fit x- and y-coordinates and the azimuthal angle  $\psi$ .

##### 4.3.1. Theoretical predictions

We use the Stokes-Einstein and Stokes-Einstein-Debye relations [32, 33] to model the translational and rotational diffusion of the Janus particles, which are approximately spherical:

$$D_t' = k_B T / 6\pi\eta a \quad (14)$$

$$D_r' = k_B T / 8\pi\eta a^3 \quad (15)$$

Because the hydrodynamic radii of polymer particles—like the PS core in our Janus particle—tend to be larger than the radii measured optically or with electron microscopy due to charged or hairy surfaces [34, 35], we do not directly compare the measured diffusion coefficients to values predicted from the theory. Instead, we calculate the effective radius  $a_{\text{eff}}$  from both the measured translation and rotational diffusion coefficients using Equations (14) and (15). We then compare these values to the best-fit diameter from the holograms and to each other.

Quantity	Experiment	Expected	Source
$a$ (nm)	$501 \pm 19$	$500 \pm 50$	SEM
$b$ (nm)	$1079 \pm 72$	$1000 \pm 100$	SEM
$n$	$1.495 \pm 0.012$	$\leq 1.54$	bulk value
$D_t$ ( $\times 10^{-13} \text{ m}^2 \text{ s}^{-1}$ )	$0.298 \pm 0.026$	$0.297 \pm 0.016$	spherocylinder model
$D_r$ ( $\text{s}^{-1}$ )	$0.311 \pm 0.034$	$0.311 \pm 0.017$	spherocylinder model
$D_{\parallel}/D_{\perp}$	$1.04 \pm 0.05$	1.13	cylinder model

Table 1: Measured and expected values of parameters for silica rods. Theoretical predictions for the spherocylinder model are based on relations in reference [27], and those for the cylinder model on relations in reference [30].

#### 4.3.2. Translational diffusion

To determine the translational diffusion coefficients for the Janus particle, we ignore the translational motion in the direction parallel to the imaging axis ( $z$ -axis) because the polar angle  $\theta$  has an uncertainty that affects the best-fit  $z$ -position, as discussed previously. We treat the Janus particle as a sphere and calculate the translational diffusion coefficient from the mean-square displacement projected onto the  $x - y$  plane:

$$\langle \Delta x^2(\tau) + \Delta y^2(\tau) \rangle = 4D_{\perp, \text{Janus}}\tau + 4\epsilon^2 \quad (16)$$

where  $\epsilon$  is the tracking precision.

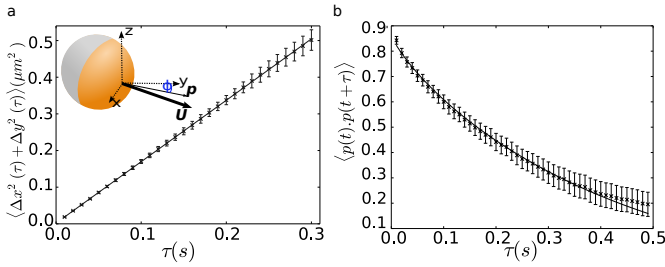


Figure 8: (a) Measured mean-square displacement of the Janus particle in the axes perpendicular to the imaging axis. The solid line is a fit to  $4D\tau + 4\epsilon^2$ . (b) Measured autocorrelation of the particle's projected orientational unit vector  $\mathbf{p}$ . The solid line is a fit to an multi-exponential decay.

By fitting the mean-square displacement to a linear model, we obtain  $D_{\perp, \text{Janus}} = 0.419 \pm 0.003 \mu\text{m}^2/\text{s}$  (see Figure 8). We then use Equation 14 at  $21 \pm 2^\circ\text{C}$  to obtain an effective particle radius  $a_{\text{eff}} = 524 \pm 15 \text{ nm}$ , which is larger than the optical radius from holography ( $443 \pm 20 \text{ nm}$  for bare polystyrene,  $490 \pm 20 \text{ nm}$  with the  $\text{TiO}_2$  layer). As discussed above, the larger hydrodynamic radius is expected for polymer particles [34, 35]. These results are summarized in Table 2.

We obtain a tracking precision of  $\epsilon = 21.8 \text{ nm}$  from the fits for the directions perpendicular to the imaging axis, which is smaller than the size of one voxel (approximately  $35 \text{ nm}$ ) and again on par with the tracking precision of complex scatterers such as spheres in clusters [13, 15].

#### 4.3.3. Rotational diffusion

Although the best-fit polar angle  $\theta$  is unreliable, we can extract the rotational diffusion coefficients from the data by considering only the azimuthal angle  $\psi$ . To do this, we derive an expression for the autocorrelation of the projection of the orientational unit vector onto the  $x - y$  plane  $\mathbf{p}(t) = \cos \psi(t) \hat{\mathbf{x}} +$

$\sin \psi(t) \hat{\mathbf{y}}$ :

$$\langle \mathbf{p}(t) \cdot \mathbf{p}(t + \tau) \rangle = \frac{1}{4} \sum_{\ell=1}^{\infty} \frac{2\ell + 1}{\ell(\ell + 1)} (S_{\ell}^1)^2 \exp[-\ell(\ell + 1)D_r\tau]. \quad (17)$$

where  $S_{\ell}^1 \equiv \int_{-1}^1 P_{\ell}^1(x) dx$  and  $P_{\ell}^1(x)$  are associated Legendre polynomials of order 1 (see Appendix for further details). This expression is a multiexponential that depends on  $D_r$  and can be evaluated numerically.

To determine the rotational diffusion coefficient we fit Equation 17 to the data and obtain  $D_{r, \text{Janus}} = 1.15 \pm 0.05 \text{ s}^{-1}$  (see Figure 8). From Equation 15 and a temperature of  $21 \pm 2^\circ\text{C}$ , we calculate an effective particle radius of  $a_{\text{eff}} = 523 \pm 6 \text{ nm}$ , in excellent agreement with the  $a_{\text{eff}} = 524 \pm 15 \text{ nm}$  obtained from translational motion. These results are summarized in Table 2. The quantitative agreement between the hydrodynamic radii calculated from the translational and rotational diffusion coefficients demonstrates the internal consistency of our fitting method, showing that the technique can effectively track the rotation and translation of Janus particles in water, despite the small asymmetry of the particles and holograms.

Although we do not use the  $z$ -coordinate or the polar angle  $\theta$  to obtain these results, they would nonetheless be difficult to obtain with a traditional optical microscope. The particles diffuse rapidly, moving more than  $5 \mu\text{m}$  in  $z$  throughout the trajectory, which might take them too far out of focus during a 2D microscopic measurement. Furthermore, the fit to the scattering model allows a quantitative determination of the azimuthal angle with no calibration required. Tracking this angle could be useful in other studies, for example to determine how quickly a particle orients in response to an external field or another object.

## 5. Conclusions and future work

We have shown a new technique to measure the 3D translational and rotational dynamics of colloidal particles. Our results show that holographic microscopy can capture the 3D position and orientation of non-spherical colloidal particles, and that these variables can be tracked precisely by fitting scattering models based on the discrete dipole approximation to the measured holograms. The technique has high precision and temporal resolution, as evidenced by the measured rotational diffusion coefficient for the Janus particle, which is an order of magnitude larger than previously measured 3D diffusion coefficients of a freely-diffusing particle.



Quantity	Experiment	Expected	Source
$a_{\text{Janus}}$ (nm)	$443 \pm 20$	$450 \pm 50$	SEM
$t$ (nm)	$47 \pm 8$	50	deposition parameters
$n_{\text{TiO}_2}$	$2.74 \pm 0.23$	2.3–2.8	bulk value
$n_{\text{PS}}$	$1.581 \pm 0.046$	$\leq 1.585$	bulk value
Translational $a_{\text{eff}}$ (nm)	$524 \pm 15$	–	
Rotational $a_{\text{eff}}$ (nm)	$523 \pm 6$	–	

Table 2: Measured and expected values of parameters for Janus particles.

We can address many of the limitations of our approach by improving our DDA implementation and fitting procedure. We intend to improve the accuracy of the measurements by antialiasing the voxelation and incorporating near-field corrections to the scattering calculations, as described in reference [36]. Spurious fits might be suppressed with an additional fitting pass that enforces a physically plausible trajectory, perhaps assisted by a Kalman filter [37].

Because the DDA is applicable to scatterers with arbitrary size, shape, and refractive index profiles, our technique could be used to measure the dynamics of a wide variety of particles. This makes it suitable for a number of different applications, including microrheology, measurements of interactions between non-spherical particles, and fundamental studies of colloidal self-assembly and bacterial motion.

## Acknowledgments

We thank Jennifer A. Lewis for helpful discussions, and feedback on this manuscript.

This work was funded by the Harvard MRSEC through NSF grant no. DMR-0820484. Scattering calculations and hologram fitting were performed on the Odyssey cluster, managed by the Harvard FAS Sciences Division Research Computing Group.

SR and IK acknowledge support from the National Science Foundation through awards CBET-1067501 and CBET-1264550. AW thanks The University of Sydney Travelling Scholarship for support. TD acknowledges support from a National Science Foundation Graduate Research Fellowship. KC was supported by the AFOSR MURI award FA9550-12-1-0471.

## Appendix A. Projection Correlation Function $\langle \mathbf{p}(t) \cdot \mathbf{p}(t + \tau) \rangle$

In this Appendix, we derive Eq. 17, with which we measure the rotational diffusion coefficient  $D_r$  of a Janus particle in Sec. 4.3.

The isotropic rotational diffusion of a particle can be quantified by studying the trajectory on the unit sphere of a unit vector  $\mathbf{u}$  fixed to the particle. Computing the autocorrelation  $\langle \mathbf{u}(t) \cdot \mathbf{u}(t + \tau) \rangle$ , where  $\tau$  is a lag time, from experimental data allows the measurement of the rotational diffusion coefficient  $D_r$ . This requires tracking the entire 3D orientation of the particle. Here we consider how  $D_r$  can be measured when only

a two-dimensional azimuthal projection of  $\mathbf{u}$  is observed, as is the case for the Janus particles.

In our experiments, we observe the normalized projection of  $\mathbf{u}$  onto the laboratory  $x - y$  plane, which is perpendicular to the optical axis. In spherical polar coordinates, where the tip of  $\mathbf{u}(t)$  has coordinates  $\theta(t)$  and  $\psi(t)$  on the unit sphere, this projection is given by  $\mathbf{p}(t) = \cos \psi(t) \hat{\mathbf{x}} + \sin \psi(t) \hat{\mathbf{y}}$ . From the data, we can then compute the autocorrelation of  $\mathbf{p}(t)$ :

$$\langle \mathbf{p}(t + \tau) \cdot \mathbf{p}(t) \rangle = \langle \cos(\psi(t + \tau)) \cos(\psi(t)) + \sin(\psi(t + \tau)) \sin(\psi(t)) \rangle. \quad (\text{A.1})$$

To simplify the notation, we will use primes to denote angles at time  $t + \tau$ ; the unprimed angles  $\theta$  and  $\psi$  are at time  $t$ . Thus,

$$\langle \mathbf{p}(t + \tau) \cdot \mathbf{p}(t) \rangle = \langle \cos \psi' \cos \psi + \sin \psi' \sin \psi \rangle. \quad (\text{A.2})$$

We show that  $D_r$  can be determined from experimental measurements of  $\langle \mathbf{p}(t + \tau) \cdot \mathbf{p}(t) \rangle$  by calculating this autocorrelation for a particle undergoing isotropic rotational diffusion characterized by  $D_r$ . We neglect translation-rotation coupling and therefore ignore the translational diffusion of the particle. Let  $f(\theta, \psi; t) d\Omega$  be the probability of finding  $\mathbf{u}$  in the solid angle  $d\Omega$  near  $(\theta, \psi)$  at time  $t$ . The probability density  $f$  is governed by a rotational Fick's law [38]:

$$\frac{\partial f}{\partial t} = D_r \left( \frac{1}{\sin \theta} \frac{\partial}{\partial \theta} \left( \sin \theta \frac{\partial f}{\partial \theta} \right) + \frac{1}{\sin^2 \theta} \frac{\partial^2 f}{\partial \psi^2} \right). \quad (\text{A.3})$$

The operator on the right is the Laplacian on the unit sphere. Computing  $\langle \mathbf{p}(t + \tau) \cdot \mathbf{p}(t) \rangle$  requires knowing the transition probability density  $K(\theta, \psi, \theta', \psi'; \tau)$  for  $\mathbf{u}$  to move from  $(\theta, \psi)$  to  $(\theta', \psi')$  after a lag time  $\tau$ . If we assume that the distribution of initial orientations  $(\theta, \psi)$  is uniform, such that  $f = 1/(4\pi)$ , then using Eq. A.2 the autocorrelation of  $\mathbf{p}$  will be given by [38]

$$\langle \mathbf{p}(t) \cdot \mathbf{p}(t + \tau) \rangle = \iint (\cos \psi \cos \psi' + \sin \psi \sin \psi') \frac{K(\theta, \psi, \theta', \psi'; \tau)}{4\pi} d\Omega d\Omega'. \quad (\text{A.4})$$

The transition probability  $K$  is given by the probability density  $f(\theta', \psi'; \tau)$ , governed by Eq. A.3, with the following initial condition:

$$f(\theta', \psi'; 0) = \frac{\delta(\theta' - \theta) \delta(\psi' - \psi)}{\sin \theta'} \quad (\text{A.5})$$

where  $\delta$  denotes the Dirac delta function. Separation of variables leads to the following solution for  $K$ :

$$K(\theta, \psi, \theta', \psi'; \tau) = \sum_{\ell=0}^{\infty} C_{\ell 0} P_{\ell}(\cos \theta') \exp[-\ell(\ell+1)D_r \tau] + \sum_{\ell=1}^{\infty} \sum_{m=1}^{\ell} \sum_{p=1}^2 C_{\ell m}^{(p)} Y_{\ell m}^{(p)}(\theta', \psi') \exp[-\ell(\ell+1)D_r \tau]. \quad (\text{A.6})$$

Here,  $P_{\ell}(\cos \theta')$  is a Legendre polynomial, and the  $Y_{\ell m}^{(p)}$  are real spherical harmonics [39]:

$$Y_{\ell m}^{(p)}(\theta', \psi') \equiv \begin{cases} P_{\ell}^m(\cos \theta') \cos m\psi' & \text{if } p = 1 \\ P_{\ell}^m(\cos \theta') \sin m\psi' & \text{if } p = 2. \end{cases} \quad (\text{A.7})$$

The initial condition in Eq. A.5 results in the expansion coefficients being

$$C_{\ell 0} = \frac{2\ell+1}{4\pi} P_{\ell}(\cos \theta) \quad (\text{A.8})$$

for the azimuthally symmetric ( $m = 0$ ) terms and

$$C_{\ell m}^{(p)} = \frac{2\ell+1}{2\pi} \frac{(\ell-m)!}{(\ell+m)!} Y_{\ell m}^{(p)}(\theta, \psi) \quad (\text{A.9})$$

for the remaining terms.

Consider the first term on the right side of Eq. A.4 which contains  $\cos \psi \cos \psi'$ . By orthogonality of  $\cos \psi$  and  $\cos \psi'$ , only terms in  $K$  with  $m = 1$  and  $p = 1$  contribute to the integral. Integration over  $\psi$  and  $\psi'$  contributes two factors of  $\pi$ , and so we obtain

$$\iint \cos \psi \cos \psi' \frac{K(\theta, \psi, \theta', \psi'; \tau)}{4\pi} d\Omega d\Omega' = \sum_{\ell=1}^{\infty} \left( \frac{2\ell+1}{\ell(\ell+1)} \frac{1}{8\pi^2} \exp[-\ell(\ell+1)D_r \tau] \pi^2 \times \int P_{\ell}^1(\cos \theta) \sin \theta d\theta \int P_{\ell}^1(\cos \theta') \sin \theta' d\theta' \right). \quad (\text{A.10})$$

Integrating the remaining term of Eq. A.4 over  $\psi$  and  $\psi'$  gives exactly the same result. Defining

$$S_{\ell}^1 \equiv \int_{-1}^1 P_{\ell}^1(x) dx, \quad (\text{A.11})$$

we obtain Eq. 17 in the manuscript:

$$\langle \mathbf{p}(t) \cdot \mathbf{p}(t + \tau) \rangle = \frac{1}{4} \sum_{\ell=1}^{\infty} \frac{2\ell+1}{\ell(\ell+1)} (S_{\ell}^1)^2 \exp[-\ell(\ell+1)D_r \tau]. \quad (\text{A.12})$$

Note that  $S_{\ell}^1 = 0$  for even  $\ell$  due to the parity of  $P_{\ell}^1(x)$ . To evaluate our result numerically, we use DiDonato's recursion relation for  $S_{\ell}^1$  [40]:

$$S_{\ell+2}^1 = \frac{\ell(\ell+2)}{(\ell+1)(\ell+3)} S_{\ell}^1. \quad (\text{A.13})$$

Unlike the results obtained by prior workers on this problem, our solution can be easily computed and used to measure  $D_r$

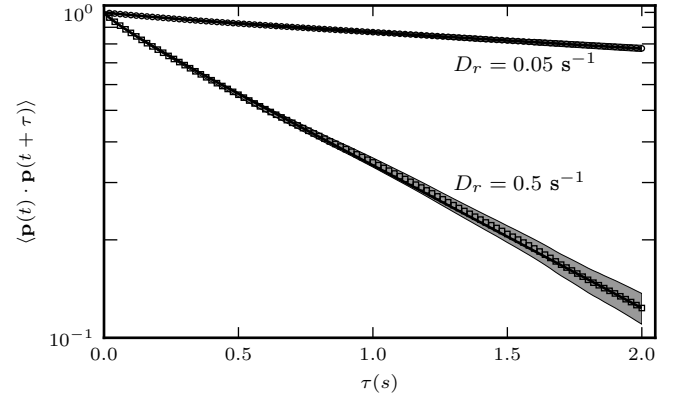


Figure A.9: Autocorrelation  $\langle \mathbf{p}(t) \cdot \mathbf{p}(t + \tau) \rangle$  for simulated particle undergoing rotational diffusion with  $D_r = 0.05 \text{ s}^{-1}$  (open circles) and  $D_r = 0.5 \text{ s}^{-1}$  (open squares). Solid lines are best fits to Eq. A.12. Shaded gray regions denote error bars on the autocorrelations, calculated using a block decorrelation technique [26].

from experimental data. Saragosti *et al.* obtain a series expression equivalent to Eq. A.12, but their solution contains complicated angular integrals that are left unevaluated [41]. They therefore determine  $D_r$  from a  $\ell = 1$  approximation of Eq. A.12. While the  $\ell = 1$  term indeed dominates when  $D_r \tau$  is large, the autocorrelation can be measured most precisely near  $\tau = 0$ , at which the number of independent angular displacements is largest. In this regime, the single-exponential approximation of Saragosti *et al.* fails, and our full solution is necessary.

We verified our result, Eq. A.12, by computing  $\langle \mathbf{p}(t) \cdot \mathbf{p}(t + \tau) \rangle$  for simulated rotational trajectories of particles undergoing rotational diffusion. We simulated rotational diffusion using the algorithm of Beard and Schlick [42]. Figure A.9 shows the autocorrelations computed from simulated trajectories with two different  $D_r$  along with fits to Eq. A.12. We find excellent agreement between the simulated autocorrelations and best fits to Eq. A.12; the values of  $D_r$  determined from the best fits agree with the simulation input values to 0.5% or better.

## References

- [1] D. A. Weitz, J. S. Huang, M. Y. Lin, J. Sung, Dynamics of diffusion-limited kinetic aggregation, *Physical Review Letters* 53 (17) (1984) 1657–1660.
- [2] S. C. Glotzer, M. J. Solomon, N. A. Kotov, Self-assembly: From nanoscale to microscale colloids, *AIChE Journal* 50 (12) (2004) 2978–2985.
- [3] P. L. Biancaneello, J. C. Crocker, Line optical tweezers instrument for measuring nanoscale interactions and kinetics, *Review of Scientific Instruments* 77 (11) (2006) 113702.
- [4] D. T. Chen, E. R. Weeks, J. C. Crocker, M. F. Islam, R. Verma, J. Gruber, A. J. Levine, T. C. Lubensky, A. G. Yodh, Rheological microscopy: Local mechanical properties from microrheology, *Physical Review Letters* 90 (10) (2003) 108301.
- [5] S. M. Anthony, L. Hong, M. Kim, S. Granick, Single-particle colloid tracking in four dimensions, *Langmuir* 22 (24) (2006) 9812–9815.
- [6] G. L. Hunter, K. V. Edmond, M. T. Elsesser, E. R. Weeks, Tracking rotational diffusion of colloidal clusters, *Optics Express* 19 (18) (2011) 17189–17202.
- [7] D. J. Kraft, R. Wittkowski, B. t. Hagen, K. V. Edmond, D. J. Pine, H. Löwen, Brownian motion and the hydrodynamic friction tensor for

- colloidal particles of arbitrary shape, *Physical Review E* 88 (5) (2013) 050301.
- [8] T. M. Kreis, Frequency analysis of digital holography with reconstruction by convolution, *Optical Engineering* 41 (8) (2002) 1829–1839.
  - [9] F. C. Cheong, D. G. Grier, Rotational and translational diffusion of copper oxide nanorods measured with holographic video microscopy, *Optics Express* 18 (7) (2010) 6555–6562.
  - [10] Y. Pu, H. Meng, Intrinsic aberrations due to Mie scattering in particle holography, *Journal of the Optical Society of America A* 20 (10) (2003) 1920–1932.
  - [11] F. C. Cheong, B. J. Krishnatreya, D. G. Grier, Strategies for three-dimensional particle tracking with holographic video microscopy, *Optics Express* 18 (13) (2010) 13563–13573.
  - [12] S. H. Lee, Y. Roichman, G. R. Yi, S. H. Kim, S. M. Yang, A. van Blaaderen, P. van Oostrum, D. G. Grier, Characterizing and tracking single colloidal particles with video holographic microscopy, *Optics Express* 15 (2007) 18275–18282.
  - [13] J. Fung, K. E. Martin, R. W. Perry, D. M. Kaz, R. McGorty, V. N. Manoharan, Measuring translational, rotational, and vibrational dynamics in colloids with digital holographic microscopy, *Optics Express* 19 (9) (2011) 8051–8065.
  - [14] J. Fung, V. N. Manoharan, Holographic measurements of anisotropic three-dimensional diffusion of colloidal clusters, *Physical Review E* 88 (2) (2013) 020302.
  - [15] R. W. Perry, G. Meng, T. G. Dimiduk, J. Fung, V. N. Manoharan, Real-space studies of the structure and dynamics of self-assembled colloidal clusters, *Faraday Discussions* 159 (2012) 211–234.
  - [16] D. W. Mackowski, M. I. Mishchenko, Calculation of the T matrix and the scattering matrix for ensembles of spheres, *Journal of the Optical Society of America A* 13 (11) (1996) 2266–2278.
  - [17] E. M. Purcell, C. R. Pennypacker, Scattering and absorption of light by nonspherical dielectric grains, *The Astrophysical Journal* 186 (1973) 705–714.
  - [18] K. Chaudhary, Q. Chen, J. J. Juárez, S. Granick, J. A. Lewis, Janus colloidal matchsticks, *Journal of the American Chemical Society* 134 (31) (2012) 12901–12903.
  - [19] A. Kuijk, A. van Blaaderen, A. Imhof, Synthesis of monodisperse, rodlike silica colloids with tunable aspect ratio, *Journal of the American Chemical Society* 133 (8) (2011) 2346–2349.
  - [20] W. Stöber, A. Fink, E. Bohn, Controlled growth of monodisperse silica spheres in the micron size range, *Journal of Colloid and Interface Science* 26 (1) (1968) 62–69.
  - [21] J. H. K. Song, I. Kretzschmar, Assembled surface-anisotropic colloids as a template for a multistage catalytic membrane reactor, *ACS Applied Materials & Interfaces* 1 (8) (2009) 1747–1754.
  - [22] D. M. Kaz, R. McGorty, M. Mani, M. P. Brenner, V. N. Manoharan, Physical ageing of the contact line on colloidal particles at liquid interfaces, *Nature Materials* 11 (2012) 138–142.
  - [23] M. A. Yurkin, A. G. Hoekstra, The discrete-dipole-approximation code ADDA: capabilities and known limitations, *Journal of Quantitative Spectroscopy and Radiative Transfer* 112 (13) (2011) 2234–2247.
  - [24] J. Fung, R. W. Perry, T. G. Dimiduk, V. N. Manoharan, Imaging multiple colloidal particles by fitting electromagnetic scattering solutions to digital holograms, *Journal of Quantitative Spectroscopy and Radiative Transfer* 113 (18) (2012) 2482–2489.
  - [25] F. C. Cheong, B. Sun, R. Dreyfus, J. Amato-Grill, K. Xiao, L. Dixon, D. G. Grier, Flow visualization and flow cytometry with holographic video microscopy, *Optics Express* 17 (15) (2009) 13071–13079.
  - [26] H. Flyvbjerg, H. G. Petersen, Error estimates on averages of correlated data, *Journal of Chemical Physics* 91 (1) (1989) 461–466.
  - [27] I. Martchenko, H. Dietsch, C. Moitzi, P. Schurtenberger, Hydrodynamic properties of magnetic nanoparticles with tunable shape anisotropy: Prediction and experimental verification, *Journal of Physical Chemistry B* 115 (49) (2011) 14838–14845.
  - [28] T. Yoshizaki, H. Yamakawa, Dynamics of spheroid-cylindrical molecules in dilute solution, *Journal of Chemical Physics* 72 (1) (1980) 57.
  - [29] T. Norisuye, M. Motowoka, H. Fujita, Wormlike chains near the rod limit: Translational friction coefficient, *Macromolecules* 12 (2) (1979) 320–323.
  - [30] M. M. Tirado, C. L. Martínez, J. G. de la Torre, Comparison of theories for the translational and rotational diffusion coefficients of rod-like macromolecules. Application to short DNA fragments, *Journal of Chemical Physics* 81 (4) (1984) 2047.
  - [31] H. Brenner, Taylor dispersion in systems of sedimenting nonspherical brownian particles. I. Homogeneous, centrosymmetric, axisymmetric particles, *Journal of Colloid and Interface Science* 71 (2) (1979) 189–208.
  - [32] A. Einstein, *Investigations on the Theory of the Brownian Movement*, Dover, New York, 1956.
  - [33] P. Debye, *Polar molecules*, Dover, New York, 1929.
  - [34] M. Gittings, D. Saville, The determination of hydrodynamic size and zeta potential from electrophoretic mobility and light scattering measurements, *Colloids and Surfaces A: Physicochemical and Engineering Aspects* 141 (1) (1998) 111–117.
  - [35] J. E. Seebergh, J. C. Berg, Evidence of a hairy layer at the surface of polystyrene latex particles, *Colloids and Surfaces A: Physicochemical and Engineering Aspects* 100 (1995) 139–153.
  - [36] S. D’Agostino, P. P. Pompa, R. Chiuri, R. J. Phaneuf, D. G. Britti, R. Rinaldi, R. Cingolani, F. Della Sala, Enhanced fluorescence by metal nanospheres on metal substrates, *Optics Letters* 34 (15) (2009) 2381–2383.
  - [37] J. Fricks, L. Yao, T. Elston, M. Forest, Time-domain methods for diffusive transport in soft matter, *SIAM Journal on Applied Mathematics* 69 (5) (2009) 1277–1308.
  - [38] B. J. Berne, R. Pecora, *Dynamic light scattering: with applications to chemistry, biology, and physics*, Wiley, 1976.
  - [39] P. M. Morse, H. Feshbach, *Methods of theoretical physics*, McGraw-Hill, New York, 1953.
  - [40] A. R. DiDonato, Recurrence relations for the indefinite integrals of the associated Legendre functions, *Mathematics of Computation* 38 (158) (1982) 547.
  - [41] J. Saragosti, P. Silberzan, A. Buguin, Modeling E. coli tumbles by rotational diffusion. implications for chemotaxis, *PLoS ONE* 7 (4) (2012) e35412.
  - [42] D. A. Beard, T. Schlick, Unbiased rotational moves for rigid-body dynamics, *Biophysical Journal* 85 (5) (2003) 2973–2976.